Magnetic Tracers for Magnetic Particle Imaging: Insight on the Roles of Frequency-Sustained Hysteresis and Interactions in Quantitative Imaging

Gabriele Barrera[*], Paolo Allia, and Paola Tiberto

INRiM, Advanced Materials Metrology and Life Sciences, Torino I-10135, Italy

Magnetic hysteresis present in tracer materials for magnetic particle imaging (MPI) either by effect of the driving-field frequency or because of interactions among nanoparticles is shown to play a crucial role when such a technique is exploited to get quantitative information about the tissue section being examined. By means of simulations based on a rate-equation model, the nanoparticles are proven to display magnetic hysteresis at the operating frequencies typical of MPI even if they are superparamagnetic in quasistatic conditions. As a consequence, the system function, a quantity crucial for image reconstruction in MPI, becomes markedly different in nature and shape from the curve produced by superparamagnetic nanoparticles. Not taking into account such an effect has detrimental consequences on quantitative MPI, as evidenced by specific examples of image reconstruction involving both monodisperse and polydisperse nanoparticles. The role played in image reconstruction by magnetic dipolar interaction, no longer negligible when nanoparticles accumulate in a small volume of the tissue, is discussed within the rate-equation model.

I. INTRODUCTION

Magnetic particle imaging (MPI) is a radiation-free, noninvasive theranostic technique with highly promising applications in biomedicine [1–3]. MPI is presently at an advanced preclinical stage [4–6]; its advantages, benefits, and drawbacks are reviewed in a number of papers [7–9]. Magnetic particle imaging can be prospectively applied to enhance the spatial and temporal resolution of tumors [10,11] and in neurosurgery [12–14], vascular medicine [15,16], cell uptake monitoring, and cell tracking [17,18]; moreover, MPI can be synergically exploited together with modern techniques of precision nanomedicine, such as computed tomography [19] and magnetic hyperthermia [18,20].

MPI is based on the detection of the magnetic response of nanometer-sized magnetic particles (tracers) [2] injected in a living body as a ferrofluid and accumulated in a target tissue [21,22] or vessel [23,24]. Superparamagnetic iron oxide nanoparticles (SPIONs) are deemed to be the tracer material of choice in MPI applications [3,25], although an efficient magnetic imaging has also been achieved by exploiting tracers, which exhibit magnetic hysteresis [12,26–28].

In preclinical applications, the technique allows information to be obtained on a biological target by determining how magnetic nanoparticles are distributed in space. In many cases, such information should be as quantitative as possible. This is a strict requirement in therapeutic or diagnostic applications where MPI is exploited in synergy with other techniques of precision nanomedicine [10,29,30], in which case an accurate quantification of the tracer distribution within the target is highly desired.

MPI exploits the different behavior of magnetic tracers when the target is submitted to a markedly nonuniform static magnetic field called the bias field, which takes the value zero in a specific region called field-free point (FFP) and is strong elsewhere [1,2,31]. The cyclic magnetization of tracers placed in the FFP and submitted to an ac magnetic field of frequency approximately 25 kHz generates an easily detectable induced voltage signal [1,2,31], whose third harmonic is the quantity actually measured by many MPI setups [2,32]. In a simplified picture, i.e., considering all tracers outside the FFP as magnetically saturated by the bias field and therefore magnetically inert, the signal is directly proportional to the local concentration of tracers in the FFP; as a consequence, the spatial distribution of nanoparticles in the tissue can be obtained by suitably moving the FFP in a scanning mode over the target. However, in laboratory tests and in the preclinical practice the magnetic signal in the FFP is not only generated by the tracers present there, but also by nanoparticles placed in nearby regions of the target where the bias field is not enough to bring them to magnetic saturation [12].

In this very common case, a central role in the image reconstruction is played by a quantity called the system function (SF), which permits to evaluate the impact on the FFP voltage of the signals coming from nearby regions

*g.barrera@inrim.it

where tracers are not entirely saturated by the bias field [33–36]. The most useful features of this quantity are the following: (a) the SF contains all the relevant physics of the magnetic nanoparticles; (b) each tracer material is characterized by a specific SF, which should be exactly known in order to get precise information about the spatial distribution of magnetic nanoparticles, i.e., an efficient quantitative imaging.

The SF of a specific set of nanoparticles is typically obtained by plotting the third harmonic of the magnetization signal as a function of the bias field [32,37–39]. As an example, when the tracer material is made of genuine superparamagnetic (SP) particles, which follow Langevin's law [40,41], the SF turns out to be a real function of the field whose exact analytic expression has been recently derived [39]. The relevant point is that, independently of the actual magnetic behavior of nanoparticles, it is crucial to reconstruct the image using a SF appropriate to the actual tracer material and to the operating conditions of a specific MPI setup.

The correct SF of any tracer material can be obtained by carefully performing a characterization of the material's magnetic properties and can be used to get an accurate image reconstruction. As a matter of fact, a variety of MPI setups operating at different frequencies and/or amplitudes of the ac magnetic field are nowadays available in laboratories and in the market [12]. Moreover, a number of tracers have been either developed in labs or offered in the market [25,42–44]. In principle, for each MPI setup and each tracer material the detailed behavior of the SF should be determined at the ac field frequency corresponding to the operating conditions; however, such an ad hoc characterization is seldom done for practical reasons.

This circumstance can be detrimental to quantitative MPI. When the SF corresponding to the operating conditions of a MPI setup and to a given tracer material is not available, a simple working hypothesis is typically made (it can be assumed, for instance, that the tracer material is comprised of ideally SP nanoparticles). Clearly, such a working hypothesis should be as close to reality as possible. In this paper, it is shown that this is not the case when tracers are assumed to be still superparamagnetic at the operating frequency of a MPI setup on the sole basis of the information extracted from dc measurements.

The magnetization of a SP nanoparticle is an entirely reversible process characterized by the absence of magnetic hysteresis [40,41]. However, nanoparticles characterized as superparamagnetic by dc measurements may lose this quality at the operating frequencies typical of a MPI setup [45–47]. In fact, high-frequency magnetization of these nanoparticles is no longer a reversible process by effect of the rapid variation of the ac driving field, which interferes with the relaxation of magnetic moments, so that a frequency-sustained magnetic hysteresis loop appears [20,45–49]. The loss of the superparamagnetic features

and the ensuing change of the nanoparticle magnetization curve may have dramatic consequences on both nature and shape of the SF.

As a matter of fact, frequency-sustained magnetic hysteresis of nanoparticles is known to have an impact on many biomedical applications, such as magnetic hyperthermia and heat-assisted drug delivery [50–55]. In a recent work by our group [46], the role played in MPI by frequency-sustained hysteresis was investigated in the very special case of an infinite magnetic field gradient (by this term it is meant that the magnetic field is so high in all regions outside the FFP that all tracers there are fully saturated [46]). Under this hypothesis, only the particles present in the FFP contribute to the magnetic signal and no SF is needed to reconstruct the image. Such a simplifying assumption is widely used in the x-space image-reconstruction approach [2,56]

The present paper shows the results of simulations based on magnetic rate equations [57] and describing the realistic case of a *finite* magnetic field gradient, characteristic of all MPI setups and leading to a more complex procedure of image reconstruction [58] where the SF plays a central role. In this paper, the magnetic nanoparticles are considered as being completely immobilized in the target tissue: such an assumption is based on solid grounds, as discussed in the literature [59–61]. Immobilization allows one to exclude both translational and rotational motion of magnetic nanoparticles, so that their magnetic behavior is not affected by Brownian motion, and specifically by physical rotation of the particle axes with respect to the fluid medium [62], and is driven by the Néel relaxation time [61]. It should be remarked that the degree of immobilization of tracers is a factor directly affecting the magnetic behavior of tracers and therefore the SF. A limitation of the model is that it cannot be used to treat MPI applications where the nanoparticles are dispersed in a dynamic environment, as in angiography or blood vessel imaging [12].

In Sec. II, we show that magnetic hysteresis of tracers—arising either by the effect of the high-frequency driving field or by the presence of magnetic interactions among particles [20,45,47]—has a strong impact on the SF, drastically modifying its behavior with the bias field from the one predicted for SP particles. Making use of a well-established magnetic rate-equation approach [57,63], the frequency-sustained hysteresis of an assembly of nanoparticles with random easy axes is accurately modeled and its effects on the shape of the SF are analyzed. The detrimental consequences of an inappropriate choice of the SF on quantitative MPI are demonstrated in Secs. III and IV by means of some examples for both monodisperse and polydisperse single-core nanoparticles. The role of dipole-dipole interaction, which takes place when nanoparticles become accumulated (either by chance or by choice) in a small volume is discussed in Sec. V.

II. MAGNETIC HYSTERESIS AND THE SYSTEM FUNCTION

Usually, the magnetization of magnetite nanoparticles for MPI applications submitted to an applied magnetic field is assumed to follow the reversible, anhysteretic Langevin function [39,44,64]; such particles will be called for short *Langevin particles*. For Langevin particles, the SF is a real function of the bias field H_0 [2,39]. The SF for Langevin particles admits an analytical expression [39] very close to the absolute value of the third derivative of the Langevin function with respect to its argument [39]. An approach based on the Langevin function is justified by the fact that most tracer materials are indeed superparamagnetic around room temperature when they are operated in quasistatic conditions [41,45–47]. However, the superparamagnetic (i.e., anhysteretic) regime is determined not only by temperature and by the intrinsic properties of nanoparticles (such as the saturation magnetization M_s and the average magnetic anisotropy $< K_{\text{eff}} >$), but also by the frequency of the driving field [20,45–49,65]; in fact, when magnetic nanoparticles are driven at high frequency (approximately 25 kHz) as in MPI applications, a hysteresis loop emerges even in particles, which are superparamagnetic at very low frequency [45,46,48].

This point is made clear by using a magnetic rate-equation approach, which has already been successfully exploited in biomedical applications of nanoparticles [46,55,66,67]. In this approach, the nanoparticles are pictured as classical double-well systems (DWSs) with random easy axes, whose magnetization at and off equilibrium is obtained by solving linear equations involving the relaxation times for energy-barrier crossing [57,65]. Only Néel's relaxation is taken into account because the nanoparticles are considered to be immobilized in the tissue. The method is based on a simple description of energy-barrier crossing by effect of both temperature and magnetic field, whose accuracy and ability to provide a realistic picture of processes taking place in magnetic nanoparticles at room temperature is discussed elsewhere [57,65] and summarized in Sec, S1 of the Supplemental Material [68].

When a hysteresis loop opens, the shape of the magnetization signal $M(t)$ is strongly modified with respect to the one given by the time-dependent Langevin function (see Sec. S2 of the Supplemental Material [68]), so that all higher-order harmonics, including the third harmonic, are expected to significantly vary from the anhysteretic case.

The magnetic nanoparticles are modeled as being single core and made of magnetite (Fe_3O_4), a typical component of the SPIONs, of spheroidal shape and diameter D. The room-temperature values of the magnetic quantities are set to match the ones of real single-core particles synthesized in laboratory: $M_s = 350$ emu/cm^3 ($\equiv 3.5 \times 10^5$ A/m), $K_{\text{eff}} = 3 \times 10^5$ erg/cm^3 ($\equiv 3 \times 10^4$ J/m^3), diameter D between 11 and 15 nm. These particles are easily checked to be superparamagnetic at room temperature in quasistatic conditions. By contrast, only particles with $D = 11$ nm are still superparamagnetic when magnetically driven at $f = 25$ kHz, the critical size for the emergence of frequency-sustained hysteresis (corresponding to the transition from temperature-driven to partially field-driven behavior [47]) being $D \simeq 11.5$ nm. The nanoparticles are submitted to the combined effect of the static bias field H_0 produced by the magnetic field gradient ($H_0 = 0$ in the FFP [1,2]) and of a harmonic driving field $H(t) = H_V \cos(\omega t)$ where H_V is the vertex field [1,2], $\omega = 2\pi f$ with $f = 25$ kHz. For the sake of simplicity, in this paper the fields $H(t)$ and H_0 are considered to be collinear; although such a condition is typically not fulfilled in many present-day MPI setups, it can be achieved as well by using an arrangement of permanent magnets and coils.

The cyclic magnetization of two sets of monodisperse particles with $D = 12$ and 14 nm obtained by solving the rate equations is shown in Fig. 1 as a function of the total field $H = H_0 + H(t)$. Here, H_0 takes different values from 0 to 400 Oe at steps of 25 Oe, whilst $H_V = 100$ Oe. When $D = 12$ nm, the cyclic magnetization is still almost anhysteretic, all minor loops being very narrow and basically aligned to each other to define a sort of master curve, which is coincident with the equilibrium magnetization curve $M(H)$. Therefore, particles with $D = 12$ nm still behave as quasisuperparamagnetic particles when driven at 25 kHz.

In contrast, for $D = 14$ nm the minor hysteresis loops centred at different H_0 values take the form of a set of intertwined rings whose vertexes are only approximately superimposed to the equilibrium magnetization curve. The loop area quickly decreases with increasing H_0, so that the loops calculated for the highest H_0 values basically merge with the equilibrium line. Small differences in particle size are observed to bring about marked differences in magnetic behavior because it is the cube of the diameter (D^3), which enters the argument of the exponentials for two Néel relaxation times in the rate equations (see Sec. S3 of the Supplemental Material [68]).

The most remarkable effect of magnetic hysteresis is that an imaginary component of the third harmonic (and therefore of the SF) appears. This is a natural consequence of the lossy magnetization process, which can be represented by the presence of an imaginary component of the cyclic magnetization $M(t)$ and all its harmonics. The effect can be clearly observed in Fig. 2, where the real and imaginary parts of the third harmonic of the magnetization, obtained by solving the rate equations, are plotted as functions of H_0 for monodisperse, noninteracting particles with diameters in the 11–15 range under the driving-field frequency $f = 25$ kHz.
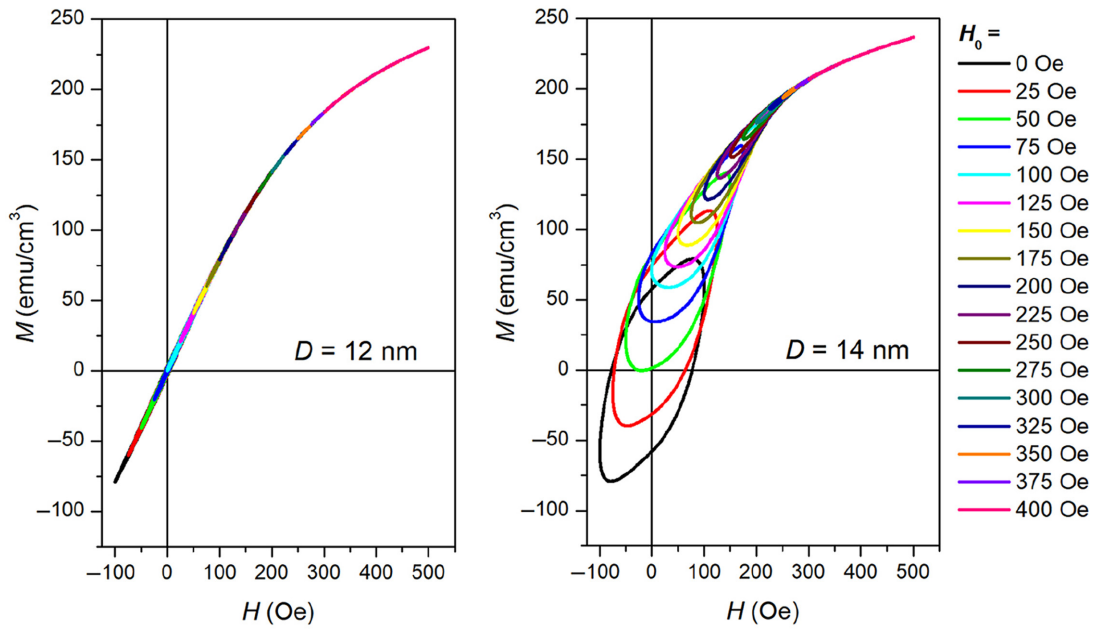
FIG. 1.   Cyclic magnetization of two monodisperse nanoparticle systems submitted to the field $H = H_0 + H_V \cos(\omega t)$ with $H_V = 100$ Oe and H_0 taking values between 0 and 400 Oe as indicated by the color list on the right. Left: quasisuperparamagnetic behavior of magnetite nanoparticles with $D = 12$ nm. Right: strongly hysteretic behavior of nanoparticles with $D = 14$ nm.

It should be remarked that particles with $D = 11$ nm still exhibit an anhysteretic magnetization at 25 kHz, whereas for all other diameters a frequency-sustained hysteresis loop opens. In fact, for $D = 11$ nm the imaginary part of the third harmonic is zero and the real part is the curve predicted by the analytical treatment of the time-dependent Langevin function [39]; the SF of nanoparticles with $D = 12$ nm—which already display a definite, if small magnetic hysteresis—still has a predominant real part. However, for larger particle sizes the imaginary part of the SF becomes comparable in magnitude to the real part, reflecting the changes in the $M(t)$ waveform arising when magnetic hysteresis appears (see Sec. S2 of the Supplemental Material [68]), and resulting in a strong deviation from the prediction for Langevin particles.

For anhysteretic particles, the SF is usually identified with the absolute value of the real $M_3(H_0)$ function [32,37–39]. Such a SF is compared in Fig. 3 to the modulus of the complex SF function obtained by taking into account magnetic hysteresis. The modulus ($|M_3|$) displays a functional behavior with H_0, which is similar to the anhysteretic case for D up to approximately 12 nm, but is rather different for larger diameters. For Langevin particles (left panel) the SF becomes zero for a single finite value of H_0, whose value depends on D; finally, it goes to zero for $H_0 \to \infty$, as expected; by contrast, in particles where magnetic hysteresis is present the real and imaginary components of M_3 become separately zero at different points of the H_0 axis (see Fig. 2), so that the modulus is always a positive quantity and becomes zero only for $H_0 \to \infty$.

A comparison between system functions helps make a useful point: while for Langevin particles the maximum value of the SF ($\mathrm{SF}_M = |M_3|_{H_0=0}$) strongly increases with increasing D, as expected [2,69], for hysteretic nanoparticles $|M_3|_{H_0=0}$ is a nonmonotonic function of D; in fact, above a critical value (close to $D = 14$ nm in the present case) $|M_3|_{H_0=0}$ decreases with further increasing D, as shown for particles with $D = 15$ nm (blue symbols on the right panel). A comparison between the two types of behavior is reported in Sec. S4 of the Supplemental Material [68]; it should be noted that $|M_3|_{H_0=0}$ gives an estimate of the sensitivity of MPI: the larger this quantity is, the higher the induced voltage signal, and the smaller the amount of nanoparticles needed to overcome the detection limit of the method.

The effect is ascribed to the fact that minor hysteresis loops in large particles become squeezed and particularly thin when D is above some critical value, which depends on the magnetic parameters (M_s, K_{eff}), as discussed elsewhere [47,70] and shown in Sec. S3 of the Supplemental Material [68], resulting in a lower overall $M(t)$ signal and in a lower magnitude of all harmonics. In fact, the rapid evolution with size of the hysteresis loops is the key factor to understand why increasing nanoparticle diameter beyond some value ceases to improve the MPI resolution and sensitivity, in contrast with the prediction for Langevin particles [2], and as actually observed [69]. In fact, the present study shows that in hysteretic nanoparticles, the maximum of $|M_3|_{H_0=0}$ occurs for an intermediate particle diameter by effect of the trade-off between the increase
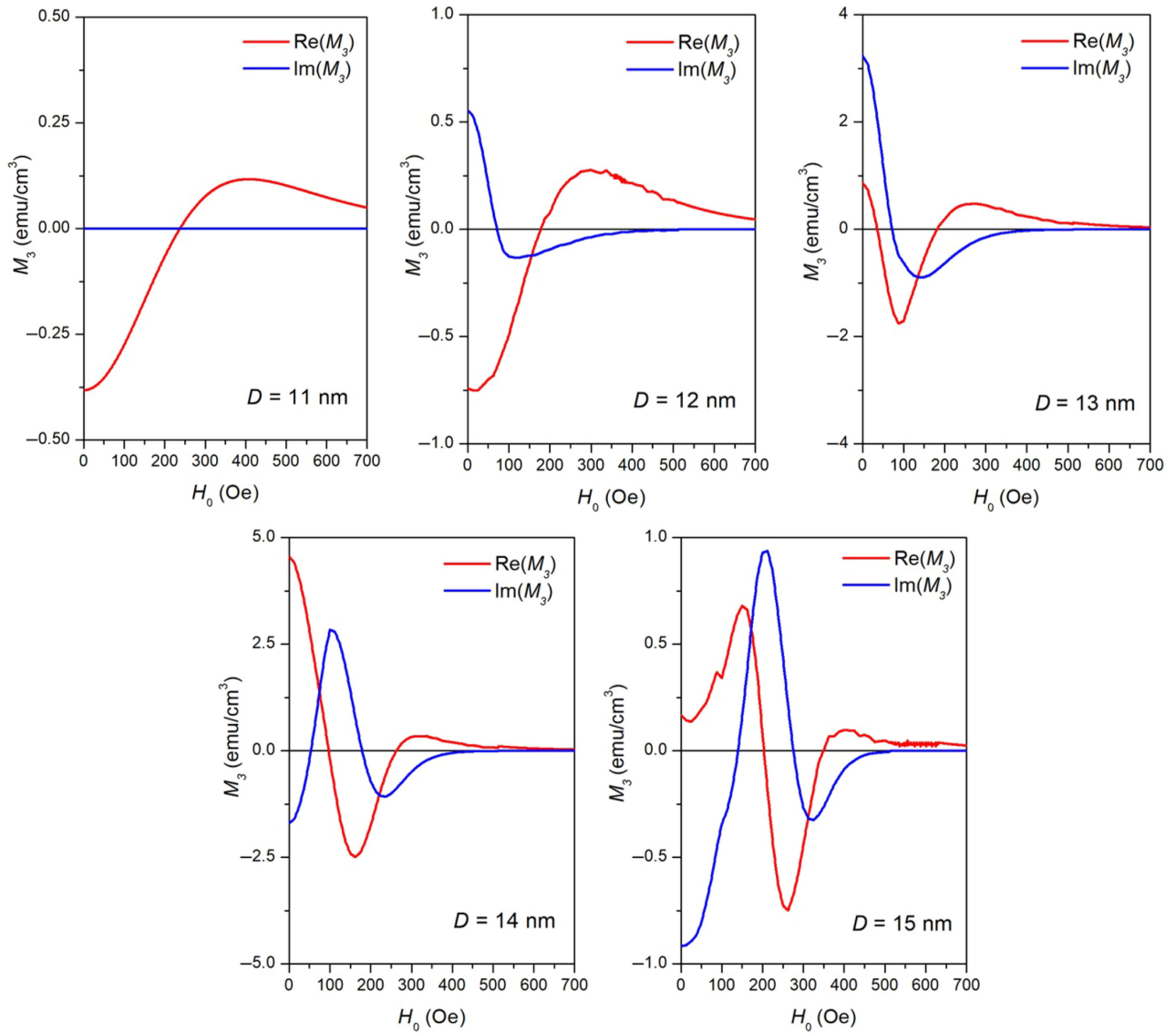
FIG. 2.   Real and imaginary parts of the third harmonic of the cyclic magnetization (M_3) as functions of the bias field H_0 for monodisperse nanoparticles characterized by magnetic hysteresis at 25 kHz (D between 12 and 15 nm); particles with $D = 11$ nm are still superparamagnetic at the operating frequency. In all cases, $H_V = 100$ Oe.

of the signal with increasing magnetic moment and the suppression of the minor hysteresis loop in large particles because of the dramatic increase of the Néel relaxation time hindering the redistribution of magnetic moments between the DWS energy minima. The maximum roughly corresponds to the widest minor hysteresis loop displayed by nanoparticles at this frequency and vertex field. The hysteresis loop is shown to be widest for a particle diameter such that the condition $\tau = 1/(2f)$ is fulfilled [55].

Of course, the diameter corresponding to the maximum of $|M_3|_{H_0=0}$ critically depends on the magnetic parameters of the modeled particles: in fact, the optimal size for MPI has been shown in simulations [71] as well as experimentally [72] to be markedly affected by magnetic anisotropy

and operation frequency and can attain slightly larger values than the one resulting in this case. In general, the condition for having an optimized MPI signal results from a delicate balance between nanoparticle size and effective anisotropy, which is in turn affected by crystal structure, shape, and surface properties of the nanoparticles. Therefore, changing the magnetic material or using multicore aggregates [73] instead of single-core particles may give rise to different numerical results without, however, affecting in a substantial way the conclusions of the present analysis.

It should be remarked that the curves shown in the left panel of Fig. 3 are not to be intended as "incorrect" with respect to the "correct" ones displayed on the right panel;
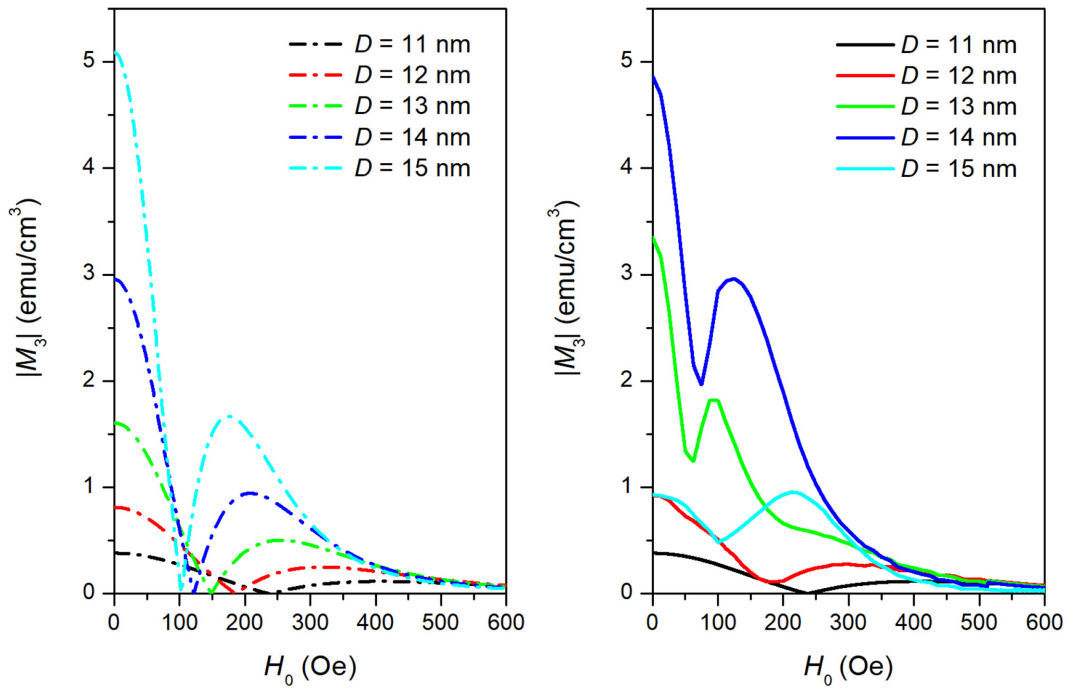
FIG. 3. Left panel: behavior with the bias field H_0 of the SF of magnetite nanoparticles with diameters between 11 and 15 nm assumed to be Langevin particles (in this case the SF admits an exact analytical representation). Right panel: the SF when frequency-sustained hysteresis is duly taken into account (in this case it is defined as the modulus of the complex M_3 function calculated from the rate equations). In all cases, $H_V = 100$ Oe.

simply, they correspond to the correct SF for the considered particles in the limit of very low frequencies (i.e., under a quasistatic driving field). This applies to commercially available magnetic ferrofluid also, where magnetic hysteresis has been measured to emerge at the typical frequencies used in MPI [73].

On the other hand, for all particle diameters exact (calculated) and Langevin-like SFs become the same at high H_0 values, as shown in Fig. 3. As a consequence, the first derivative of the standard Langevin function (often assumed to represent the point-spread function (PSF) [2,74] and used to approximately determine both the resolution and the sensitivity of the magnetic imaging process [2,75,76]) is basically not affected by magnetic hysteresis of tracers at the operating frequency. As a matter of fact, the PSF can be more accurately determined by means of experimental measurements [77] and, similar to the system function approach, can be exploited to calibrate the actual magnetization response of a nanoparticle in the scanned area and provide information for a reliable image reconstruction.

Quantitative imaging can be achieved through one of the procedures of image reconstruction, which have been recently proposed [2,58], inherently involving the correct knowledge of the the actual behavior of magnetic tracers in the operating conditions. Not taking into account the actual hysteretic features of the magnetic response of tracers can lead to an inaccurate estimate of the tracer concentration, as shown in the next section. In the present approach, the behavior of tracers is accounted for by the SF.

III. IMAGE RECONSTRUCTION USING HYSTERETIC TRACERS

The many and complex problems related to the procedure for image reconstruction in standard MPI operations are extensively discussed in the recent literature [58,78,79]. Here, a somewhat simplified description of the reconstruction procedure is considered, the focus of this paper being on the role played by the SF rather than on the practical details of the reconstruction itself. As is well known, one of the key aims of the MPI technique is to find the local concentration of magnetic tracers over a scanned area of living tissue by detecting the overall voltage induced by magnetic tracers at the FFP position.

In the following treatment, magnetic particles are assumed to be distributed according to a function $c(x_i, y_i)$ on a square of edge L lying in the (x, y) plane and subdivided in N minor square regions of edge $L/N^{1/2}$, each one labeled by the index $i = 1, 2, \ldots, N$. The following values are used: $L = 16$ cm, $N = 2025$. For the sake of simplicity, the depth of the scanned volume below the square of edge L is taken equal to one particle's diameter, in order to avoid considering the effects of the dispersion of particles along the z axis.

Both the generation of the induced voltage and the image reconstruction are described by linear algebra of matrices. The N values of the local particle concentration $c_i \equiv c(x_i, y_i)$ define the (real) vector **c**. The contribution of the ith region to the third harmonic of the induced voltage generated by tracers in the FFP is V_{3i}; the N quantities V_{3i} define the vector **V₃**, which is obtained by operating on **c** with the $N \times N$ matrix **[SF]**, assumed to be a known invertible matrix. The generic element $SF_{i,j}$ is the value taken by the SF function at position j when the FFP is at position i. By effect of the static magnetic field gradient, the i-j distance implies that the bias field (equal to zero in region i) takes some positive value H_0^* in region j; the $SF_{i,j}$ element is just the value of the SF for $H_0 = H_0^*$.

In the MPI practice, **c** is an unknown vector, which is obtained from the measured V_{3i} values by operating on **V₃** with the inverse matrix **[SF]**$^{-1}$. The SF plays, therefore, a central role in the imaging procedure. However, as has been previously pointed out, the choice of the SF used to generate both **[SF]** and **[SF]**$^{-1}$ matrices is sometimes based more upon a reasonable guess than on the detailed knowledge of its actual behavior: this is the case when the SF for Langevin particles—appropriate to tracers driven at very low frequency—is used in place of the SF emerging from the real magnetic response of tracers driven at the much higher operating frequency f. As discussed in the previous section, the difference between the actual SF and the Langevin-particle SF can be remarkable when frequency-sustained magnetic hysteresis of tracers is no longer negligible.

An effect arising from the hysteretic magnetization of tracers is the presence of an imaginary component of the system function. Therefore, in this case **[SF]** is a complex matrix resulting in a complex **V₃** vector when applied to the real **c** vector. In other words, if the induced voltage is measured to have an imaginary part (or alternatively to exhibit a phase shift different from $\pi/2$ with respect to the driving field), it can be concluded that the SF is a complex function of H_0 and that the magnetic tracers are no longer Langevin particles at the driving frequency.

An example is graphically depicted in Fig. 4. Tracers are supposed to have a size such that their cyclic magnetization at 25 kHz is hysteretic (with the parameter values used in this work, the particle diameter must be larger than 11.5 nm). The total number of tracers distributed over the scanned surface of area L^2 is such that the average surface fraction f_s is equal to 1×10^{-4}. This quantity is defined as $f_s = S_{tot}/L^2$ where S_{tot} is the sum of all areas projected on the (x, y) plane by the spherical magnetite nanoparticles (independent of their diameter). For a uniform distribution of particles on the square of edge L, the value $f_s = 1 \times 10^{-4}$ corresponds to distant nanoparticles, the ratio (d/D) between average interparticle distance d and particle diameter being as large as about 88.6, as

shown in Appendix; therefore, the particles can be safely considered as noninteracting.

An accumulation of particles around the center of the scanned region is modeled by a Gaussian function $c(x_i, y_i) \equiv c(r_i) = A \exp[-r_i^2/(2\sigma^2)]$ with $r_i = (x_i^2 + y_i^2)^{1/2}$ and standard deviation $\sigma = 0.8$ cm (see Fig. 4). By definition, the total surface of magnetite particles is $S_{tot} = \sum_{ij} c(x_i, y_j)\Delta x_i \Delta y_j$, where $\Delta x_i, \Delta y_j$ are the lengths of the edges of the minor square regions. The amplitude A is determined by equating $\sum_{ij} c(x_i, y_j)\Delta x_i \Delta y_j$ to $f_s L^2 = 256 f_s$ and turns out to be $A \simeq 256 f_s/(2\pi\sigma^2) \simeq 7 \times 10^{-3}$. It should be noted that for magnetite particles with diameters in the considered range, the value of f_s used in the example corresponds to a total mass of Fe well above the detection limit of MPI ($1 - 5 \times 10^{-9}$ g) [3,11]. Note that even within the central minor square region (where the concentration is highest) the ratio d/D is still as high as 10.6, as shown in the Appendix, so that the particles are noninteracting throughout.

In the case of hysteretic nanoparticles, the correct SF is a complex function of H_0, so that **V₃** becomes a complex vector, resulting in the modulus and phase components shown in the right panel of Fig. 4. When operating with the correct **[SF]**$^{-1}$ matrix on **V₃** (blue arrow), the starting **c** vector (which is obviously a real quantity) is perfectly recovered. In contrast, if the reconstruction is operated using the real matrix **[SF*]$^{-1}$** whose elements are given by the system function appropriate to particles of the same size assumed to be *bona fide* Langevin particles (red arrow), the unphysical result of a complex **c** vector is obtained.

A. Impact of the choice of SF on the image reconstruction

Given a **[SF]** matrix, operating on the vector **V₃** with the inverse matrix **[SF]**$^{-1}$ results by definition in the correct **c** vector. In this section we discuss the impact of an ill-defined system function on the correct reconstruction of the tracer concentration $c(r_i)$. In the present analysis, the inverse matrix is obtained by making use of the SF for Langevin particles, independently of the particle diameter. It has however been shown that this is valid for particles with $D \leq 11$ nm only. For diameters larger than 11 nm, tracers are no longer genuine Langevin particles because of frequency-sustained magnetic hysteresis. The deviation of the correct SF from the prediction of the Langevin theory [2,39] increases with increasing D.

In order to make the reconstruction numerically stable, the Tikhonov regularization [58,80] has been adopted. This is one of the many numerical techniques developed to contrast the amplification of noise inherent in the solution of inverse problems [58], and has the advantage of being well known and particularly simple to implement.
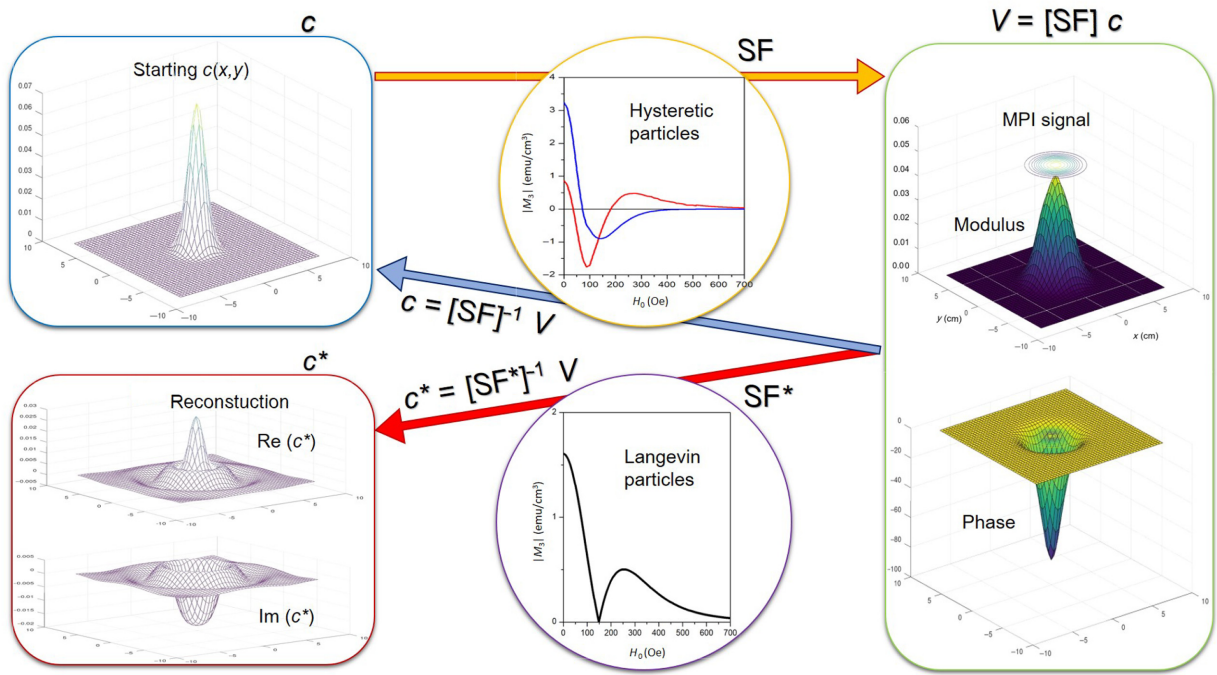
FIG. 4. Induced voltage V generated by a known planar distribution of tracers with magnetic hysteresis, $c(x, y) \equiv c(r)$ (yellow arrow pointing right). The arrows pointing left indicate two possible image reconstruction procedures. Blue arrow: reconstruction based on the correct system function for hysteretic nanoparticles. Red arrow: reconstruction based on the assumption that the particles are without hysteresis. See text for details.

The impact of an improper choice of the SF to build the $[\text{SF}]^{-1}$ matrix for tracers with D in the 12–15 nm interval is shown in Fig. 5 under an average magnetic field gradient of 3 T/m (3×10^2 Oe/cm), a value typically found in MPI setups. In the considered case, the bias field $\mathbf{H}_0(x, y, z)$ is assumed to be perpendicular to the scanned area of edge L, which lies in the (x, y) plane at $z = 0$. The magnitude of the field increases with increasing the distance from the FFP, which is at the center of the scanned area. Within each minor square region of edge $L/N^{1/2}$ the field $\mathbf{H}_0$ is considered to keep the same magnitude as at the geometric center of the considered region. The high-frequency driving field, generated by a solenoid parallel to the z axis, is perpendicular to the (x, y) plane as well.

The real (starting) Gaussian distribution of particles over the plane $c(r_i)$ is shown on top of Fig. 5 both in a three-dimensional (3D) graph representation and on a contour colour map. The modulus [81] of the distribution $c^*(r_i)$ obtained using the inverse real matrix $[\text{SF*}]^{-1}$ is shown using the same representations for all considered particle diameters. Only for $D = 12$ nm is the reconstructed $|c^*(r_i)|$ still reasonably close to the starting function in both height and width, although some minor artifacts (undulations) begin to appear at large distances from the center; for larger diameters, the behavior of the reconstructed modulus becomes more and more distant from the real distribution.

These artifacts indicate the presence of tracers in regions of the (x, y) plane where no particles actually exist. The peak of the reconstructed distribution is always at $x = 0$, $y = 0$, but it becomes increasingly lower and less significant with increasing D. When $D = 15$ nm, an operator of the MPI setup would conclude that very few tracers are present in the scanned region and that they are rather evenly distributed over the plane, which is clearly not the case.

A more quantitative insight on the effect is given by Fig. 6, where the profile of the reconstructed $|c^*(r_i)|$ distribution along the x axis in $y = 0$ is shown for particle diameters in the interval $11.5 \leq D \leq 15$ nm. The reconstruction for particles with $D < 11.5$ nm (not shown here) turns out to be a real function of x and is perfectly superimposed to the starting $c(x, 0)$ curve, as expected for particles still superparamagnetic at 25 kHz. When $D = 11.5$ nm, $c^*(x_i, 0)$ is basically still a real quantity closely corresponding to the actual concentration (red and black lines in the left panel of Fig. 6). Increasing the particle diameter brings about a strong reduction of the central peak together with increasingly larger artifacts, as shown in the left panel. A quantitative measure of the deviation of the reconstructed tracer distribution from the real one is shown in the right panel, where the standard deviation $\sigma_s = \left[\sum_{i=1}^{N} (|c^*(x_i, 0)| - c(x_i, 0))^2 \right]^{1/2}$ of the differences between reconstructed and actual c_i values is plotted. The
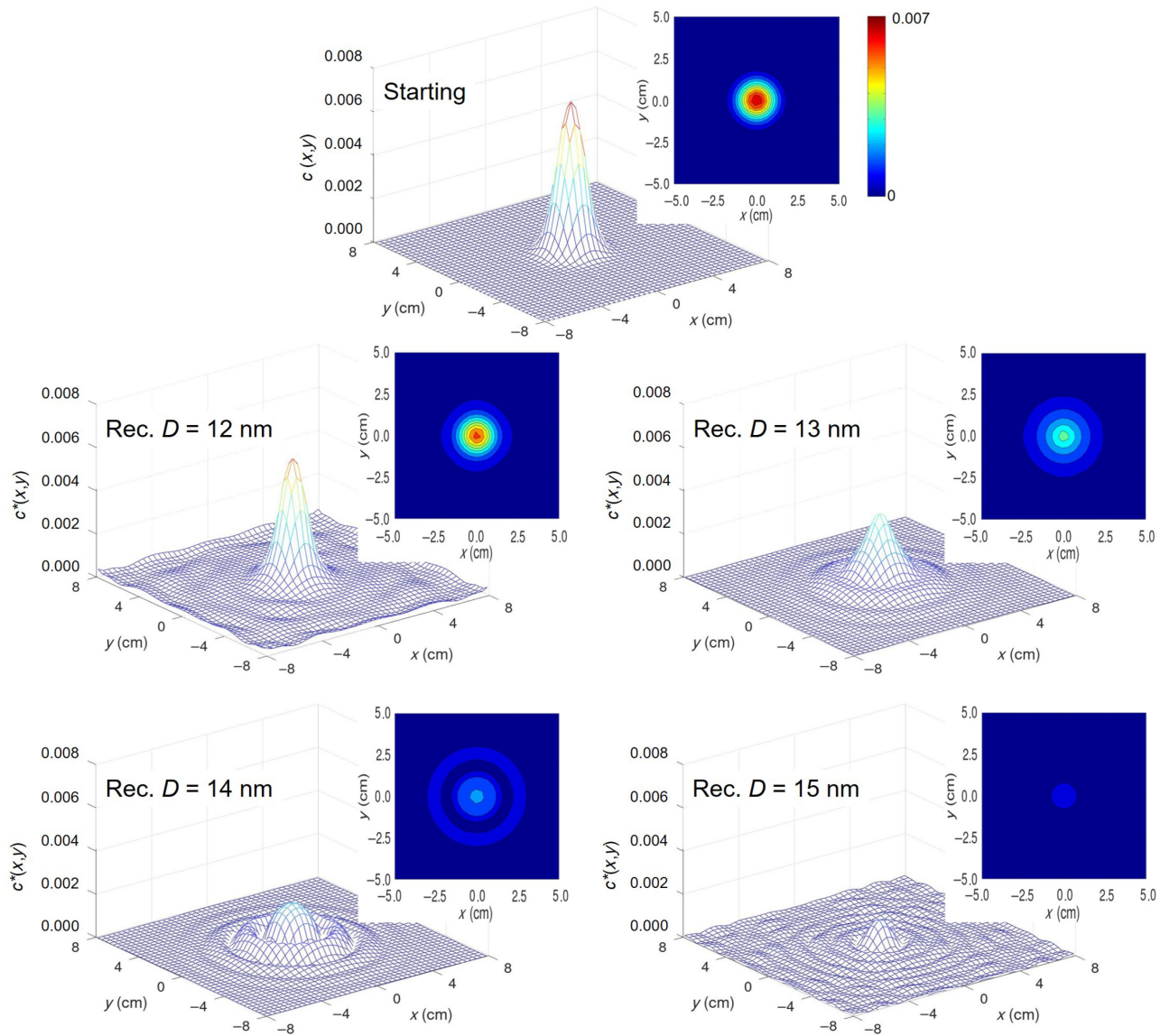
FIG. 5.   Image reconstruction under a magnetic field gradient of 3 T/m, using 3D and color-contour maps. Top center panel: starting Gaussian distribution of nanoparticles on the target. The four panels below show the reconstructed distributions for hysteretic nanoparticles of different size obtained neglecting magnetic hysteresis. The concentrations c, c^* are dimensionless quantities; the color scale shown in the top panel is the same everywhere.

standard deviation is equal to zero up to (and including) $D = 11$ nm; when magnetic hysteresis begins to play a role, a nonzero σ_s appears; the standard deviation monotonically increases with increasing D, indicating that the reconstruction becomes increasingly worse.

As shown in the Sec. S6 of the Supplemental Material [68], increasing the field gradient magnitude reduces the mismatch between the actual concentration and the one reconstructed considering hysteretic tracers as Langevin particles. This is explained recalling that in the limit of an infinite field gradient **[SF]** is a diagonal matrix, because only tracers located in the FFP contribute to the induced voltage, all particles in other regions of the scanned plane being magnetically saturated. As a consequence, the vector **c** is proportional to vector **V** and the reconstruction procedure becomes trivial [2,46]. However, the proportionality constant between the two vectors is a real number for genuine Langevin particles only, while it is a complex number in the case of hysteretic tracers. In the latter case, the modulus of the reconstructed $c^*(r_i)$ function is expected to give a correct information on the *shape* of the actual particle distribution, because the shape is intimately related to the structure of the **[SF]** matrix, which in the case of an infinite gradient is diagonal for both Langevin and hysteretic particles. However, the diagonal elements for Langevin and hysteretic particles are different, and this mismatch leads
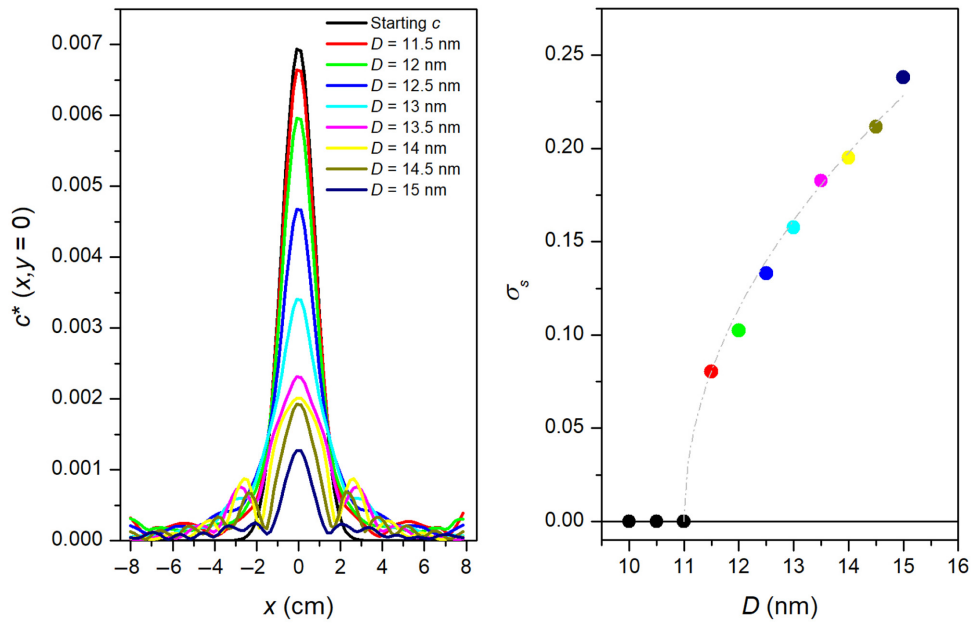
FIG. 6. Left: profile of starting and reconstructed nanoparticle distributions along the x axis, for different diameters of nanoparticles with frequency-sustained hysteresis; the reconstruction for particles still superparamagnetic at 25 kHz ($D < 11.5$ nm) is not shown, being perfectly superimposed to the starting $c(x, 0)$ curve. Right: standard deviation σ_s of the differences between reconstructed and actual distribution curves, plotted as a function of nanoparticle diameter. The dotted line is a guide for the eye.

to an incorrect quantitative estimate of the actual particle concentration at every point of the scanned surface.

B. Resolution

When the magnetization of tracers for MPI displays hysteresis at the operation frequency, making use of the inverse matrix for Langevin particles ($[\mathbf{SF^*}]^{-1}$) instead of the correct one ($[\mathbf{SF}]^{-1}$) affects the spatial resolution of MPI also. The upper panel of Fig. 7 shows the contour-color map representation of a simple bimodal distribution of particles on the (x, y) plane generated by two Gaussian functions of the same variance and amplitude symmetrically placed along the x axis close to the center of the scanned surface. The distance between the two concentration maxima is $d = 1$ cm. With this choice of parameters, the two peaks of the bimodal distribution are well separated. The following panels show the behavior of the reconstructed $|c^*(x_i, y_i)|$ functions for hysteretic particles with diameters in the 12–15 nm interval, obtained using the $[\mathbf{SF^*}]^{-1}$ inverse matrix appropriate to Langevin particles. The ability of the reconstruction procedure to resolve the two peaks becomes worse with increasing D, and artifacts indicating the presence of "phantom particles" along the perpendicular direction (the y axis) appear for $D = 13$, 14 nm. When $D = 15$ these "phantom particles" seem to disappear (at least on the z scale used in Fig. 7), but the reconstructed concentration is everywhere extremely low with respect to the actual one. It should be noted that by properly changing the z scale the "phantom particles"

appear even for $D = 15$ nm, as shown in Sec. S7 of the Supplemental Material [68].

The observed artifacts are particularly apparent in particles with $D = 13$, 14 nm because for these diameters the correct SF is substantially different from the one for Langevin particles of the same size (compare the curves in the two panels of Fig. 3), whilst the shape of $|M_3|$ for $D = 15$ nm is closer to the corresponding one for Langevin particles (although the reduced magnitude results in very low values of the induced voltage V_{3i} and in correspondingly low values of the reconstructed distribution $|c^*(x_i, y_i)|$).

IV. EFFECT OF NANOPARTICLE SIZE DISTRIBUTION

The previous results are obtained for monodisperse particles. In fact, magnetic tracer materials for MPI are typically comprised of iron-oxide nanoparticles widely distributed in size [5,11,40], resulting in the simultaneous presence of anhysteretic (Langevin-like) and hysteretic cyclic magnetization at the operation frequency, even when all particles are superparamagnetic at low frequency. This fact has been experimentally checked [73]. As a consequence, the effects discussed in the previous sections can play a non-negligible role even in materials containing size-distributed nanoparticles.

As an example, let us consider the Gaussian distribution of particle sizes $p(D)$ shown in the top left panel of Fig. 8. The mode of the distribution is set at $D = 11.5$ nm, so that with the parameter values of this work the material
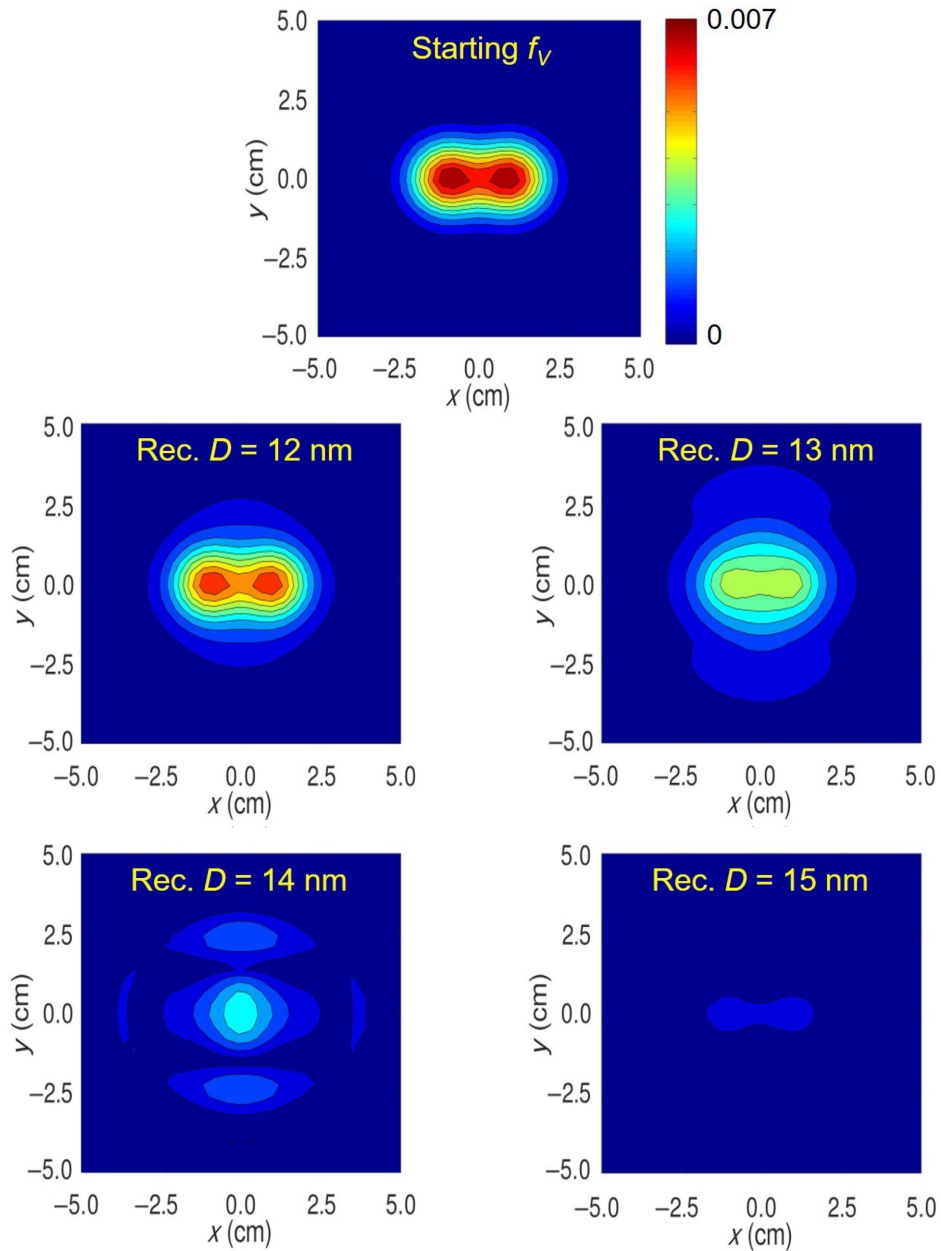
FIG. 7.   Image resolution. Top panel: contour-color map of the starting distribution of tracers on the plane; the four panels below show the reconstructed distribution for hysteretic nanoparticles of different size when magnetic hysteresis is neglected. The color scale shown in the top panel represents the nanoparticle concentration (a dimensionless quantity) and is the same everywhere.

contains exactly one half of magnetite particles, which are still superparamagnetic at $f = 25$ kHz and one half whose magnetization is hysteretic, as indicated. When the particles are noninteracting or weakly interacting, the total SF is obtained by separately summing up all the real and all the imaginary parts of the SFs appropriate to each diameter. The resulting SF is a complex function of bias field whose modulus is indicated by the red dotted line in the top right panel of Fig. 8, where it is compared to the SF obtained by assuming that *all* particles are still Langevin particles at the operating frequency, which is a real function of the

bias field (black line). Although the two curves become superimposed at large fields, they substantially differ at intermediate values of H_0, i.e., rather close to the FFP.

A reconstruction operated not taking into account the hysteretic behavior of a fraction of the tracers is therefore expected to be affected by errors. In the example of Fig. 8 the particles are assumed to be randomly distributed in space on the (x, y) plane according to the same Gaussian function $c(r_i)$ shown in the top panel of Fig. 4; in the bottom left panel of Fig. 8 the reconstructed $|c^*(r_i)|$ function obtained using the inverse real matrix $[\mathbf{SF*}]^{-1}$
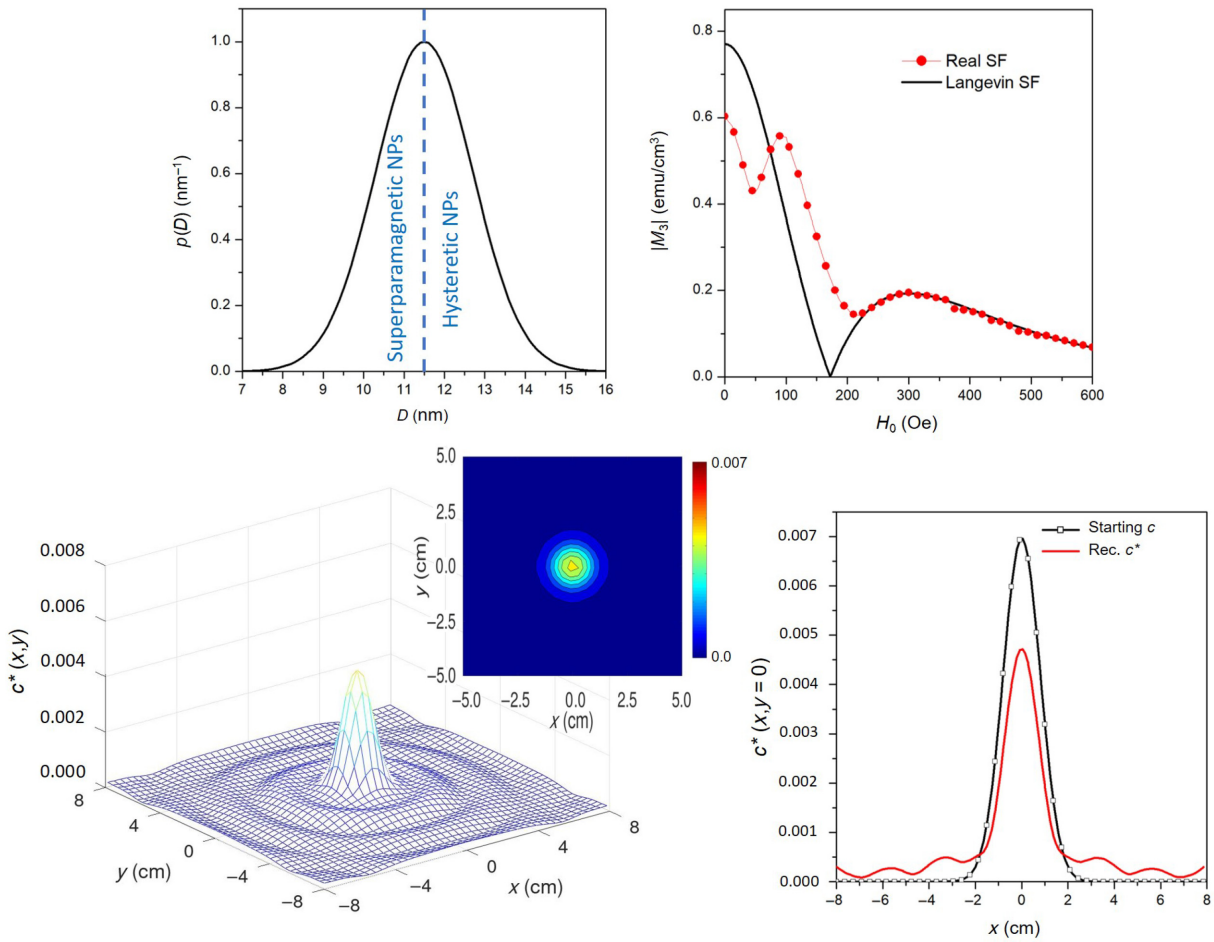
FIG. 8. Effect of tracer size distribution. Top left: size distribution of tracers with an equal number of nanoparticles with and without hysteresis at 25 kHz. Top right: real part of the actual SF compared with the SF obtained assuming that all tracers are still Langevin particles. Bottom left: reconstruction of the starting Gaussian distribution of tracers on the plane (shown in the top panel of Fig. 5) when all tracers are assumed to be Langevin particles. Bottom right: profile along the x axis evidencing the mismatch between starting and reconstructed nanoparticle distributions. The color scale represents the dimensionless nanoparticle concentration.

appropriate to Langevin particles is shown in both a 3D graph representation and on a color-contour map.

Disregarding the presence of hysteretic particles brings about an unsatisfactory reconstruction characterized by a lower peak value with respect to the real distribution and by the presence of artifacts (once again, undulations and "phantom particles") away from the center of the surface. This is put in evidence in the bottom right panel of the same figure, where the profile along x of starting ($c(x_i, 0)$) and reconstructed ($|c^*(x_i, 0)|$) distribution is compared.

V. EFFECT OF INTERPARTICLE INTERACTION

In the rate equations' framework, the effect of dipolar volume interactions among particles is modeled as an increase of the energy barrier between the two energy minima of a DWS [47,67]. Introducing dipolar interaction results in a complex behavior (i.e., either an enhancement or a reduction, depending on particle size) not only of the

hysteresis loop width [47] but also of $|M_3|$ [46]. The effect on the amplitude of the third harmonic is discussed in Sec. S5 of the Supplemental Material [68]. As a consequence, the SF is expected to be markedly affected by interparticle interaction.

In a cyclic magnetization process, dipole-dipole energy depends on the degree of alignment of magnetic dipoles and is assumed to oscillate between a maximum and a minimum, the latter being about one half of the former [47]. The maximum rms dipolar energy is

$$E_D^{\max} = \alpha \frac{\mu^2}{d^3}, \tag{1}$$

where α is a dimensionless quantity of the order of 10 [47, 82], and $\mu = M_s V$ is the magnetic moment carried by a particle of volume V having spontaneous magnetization M_s

[47]. In three dimensions, E_D^{max} can be written as [47]

$$E_D^{\mathrm{max}} = \alpha M_s^2 V f_V, \qquad (2)$$

where $f_V = V/d^3$ is the volume fraction of nanoparticles. In two dimensions, Eq. (1) transforms into

$$E_D^{\mathrm{max}} = \frac{8}{\pi^{1/2}} \alpha_2 M_s^2 V f_s^{3/2}, \qquad (3)$$

where f_s is the surface fraction defined in Sec. III and the relation $(1/d) = 2f_s^{1/2}/(\pi^{1/2}D)$ is exploited (see Appendix). The dimensionless parameter α_2 is smaller than α because the particles are distributed over a plane rather than in a volume (see Appendix); in particular, $\alpha_2 \simeq 0.745\,\alpha$.

The effect of dipolar interaction on the SF is shown in the two upper panels of Fig. 9 for a uniform distribution of particles on the scanned plane, considering different values of f_s and two nanoparticle diameters. The limits of the investigated interval of the surface fraction f_s (0.02

and 0.1) correspond to (d/D) values between 6.3 and 2.8, respectively. The curves for noninteracting particles are added for comparison. For 13-nm tracers, an increase of f_s brings about first an enhancement of the SF at $H_0 = 0$ and in general of the whole curve; however, above $f_s \simeq 0.06$ the trend is inverted and a reduction of the SF is observed. Such a behavior of the magnitude of $|M_3|$ is associated with a smoothing of both the secondary maximum and the dip of the curve. In contrast, for 14-nm tracers a monotonic reduction of the magnitude of the SF with respect to the noninteracting case is observed, along with a smoothing of the whole curve; for this diameter, the secondary maximum is observed to become higher than the value at $H_0=0$. For both diameters, the tails of all curves become almost coincident at large H_0 with the one describing noninteracting particles.

It may be interesting to compare the behavior of the SF obtained by our simulations for a non-negligible interaction among particles ($f_s > 0.06$) with the results obtained in Ref. [27], where interparticle interaction is so strong that short nanoparticle chains are formed; the magnetization
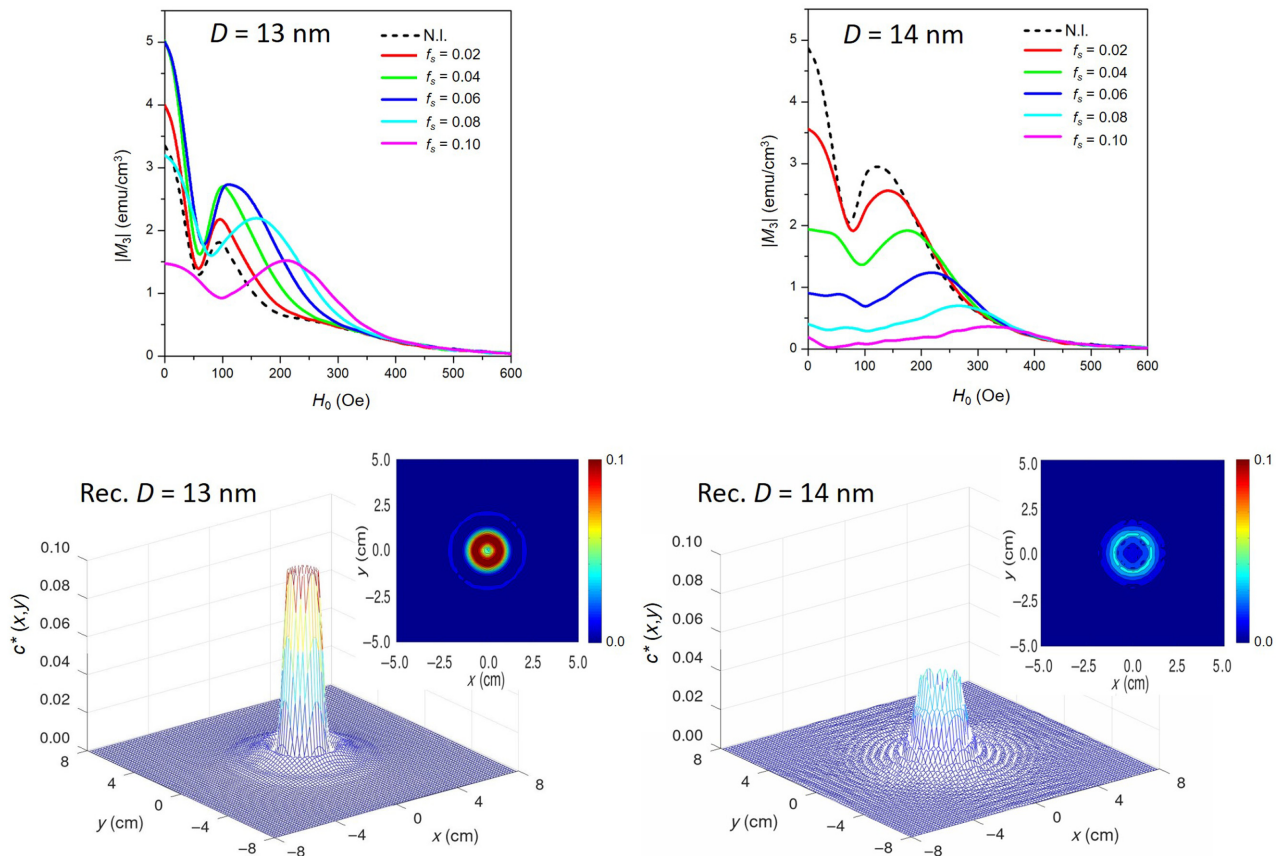

FIG. 9.   Effect of dipole-dipole interaction. Top panels: change of the SF by effect of an increasing surface fraction of nanoparticles for two diameters; the noninteracting case corresponds to $f_s = 0$. Bottom panels: reconstructed images of a Gaussian distribution of interacting particles ($f_s = 0.1$) on the plane (shape as in the top panel of Fig. 5) obtained neglecting the interaction. The color scale represents the dimensionless nanoparticle concentration.

of the chain coherently rotates giving rise to a wide hysteresis loop and to a strong MPI signal at the coercive field. In both cases, dipolar interaction plays a considerable role, leading to a strong contribution to the picked-up signal at a field different from zero (i.e., not at the FFP). This effect is to be duly taken into account in MPI image reconstruction.

It is interesting to note that when dipolar interaction among nanoparticles of a given diameter is switched on, the SF becomes similar to the one calculated for noninteracting particles of slightly larger diameter. As an example, let us consider the effect of the interaction existing when $f_s = 0.06$ (blue lines in Fig. 9). For $D = 13$ nm, the SF has a shape similar to the one of noninteracting particles with $D = 14$ nm (blue line in the right panel of Fig. 3), whereas for $D = 14$ nm, the shape of the SF is similar to the one of noninteracting particles with $D = 15$ nm (line in cyan in the right panel of Fig. 3). This effect can be explained by considering that dipolar interaction brings about an increase of the energy barrier between minima of the DWS with respect to the noninteracting case [47]; the energy barrier being proportional to V [83], a higher E_B can be interpreted as a virtual increase of the size of the particles, thought to be noninteracting.

When dipolar interaction cannot be disregarded, neglecting the effects of dipole-dipole interaction affects image reconstruction, as shown in the two lower panels of Fig. 9. In this case, the average surface fraction f_s is assumed to be as large as 1.57×10^{-3}; this means that the number of nanoparticles dispersed on the scanned plane is such that they can no longer be considered as noninteracting. As in Sec. III, nanoparticles are assumed to accumulate around the center of the scanned region. The accumulation is described by the Gaussian function of Sec. III with the same standard deviation σ but a much larger amplitude ($A = 0.1$ instead of 7×10^{-3}). The lower right panel shows the reconstructed image obtained using the inverse matrix for ideally noninteracting particles instead of the correct one. It should be noted that in the case of interacting nanoparticles the local surface fraction $f_s^{(j)}$ present in each region j of the scanned plane plays a complex role on the value of each matrix element $SF_{i,j}$, which is determined not only by the number of particles in region j (given by $f_s^{(j)} \Delta x_j \Delta y_j$) but also by the local value of the energy barrier for the DWS, which in turn depends on $f_s^{(j)}$ through Eq. (3).

As a consequence, for both particle diameters the reconstructed $|c^*(r_i)|$ curve turns out to be quite different—both in shape and maximum amplitude–from the starting Gaussian function. In fact, for the examined diameters the reconstructed concentration of tracers has a dip instead of a maximum at the center of the scanned area. This is explained considering that in the central minor square region the tracer concentration and the interaction are highest (there, $f_s = 0.1$, corresponding to $d/D \simeq 2.8$), and the

SF is strongly reduced in both cases (see upper panels of Fig. 9). Even in this case, "phantom particles" appear at large distances from the center because of the undulating behavior of the reconstructed $|c^*(r_i)|$ function. Note that for $D = 14$ nm $|c^*(r_i)|$ is everywhere very small compared to to the starting $|c(r_i)|$ function, in agreement with the strong monotonic decrease of the system function with increasing f_s, shown in the upper right panel.

VI. CONCLUSIONS

We show how the magnetic properties of tracers can affect magnetic particle imaging by influencing the system function associated to a specific tracer material and the image reconstruction, which is based on it. Using rate equations, we explain why the SF critically depends on the actual magnetic behavior of tracers at the driving-field frequency, pointing out the relevance of carefully characterizing the magnetic nanoparticles at the operating frequency in order to guarantee the optimal efficiency of a MPI setup.

Generally speaking, a detailed knowledge of the actual magnetic behavior of nanoparticles is mandatory not only in magnetic imaging but also in other recent biomedical applications. In the specific case of MPI, where nanoparticles are submitted to a driving field of medium-high-frequency, magnetic hysteresis cannot be disregarded because frequency-sustained hysteresis loops may appear even in particles, which are superparamagnetic at very low frequency.

Although Brownian relaxation is not taken into account in the rate-equation framework, a core point of the present paper is the recognition of the problems arising when the SF of superparamagnetic particles is unduly exploited in image reconstruction. Physical rotation of particle axes further increases the width of the loop resulting from Néel's relaxation [73]. An evolution of the present rate-equation model, able to add the effect of physical rotation of the particle axes, would allow the prediction of a more realistic SF of particles, which are not rotationally immobilized.

Magnetic hysteresis modifies the SF to such an extent that approximating the actual magnetization process of nanoparticles through a simplified picture can be detrimental in all applications where quantitative information of the tracer distribution in a tissue has to be obtained. In any case, the reversible magnetization typical of superparamagnetism is by no means a mandatory requirement for an efficient magnetic imaging.

In the presence of magnetic hysteresis, the SF is no longer a simple real function of the bias field. In fact, a nonzero phase angle between magnetization and driving-field signals (or, alternatively, a phase angle not equal to $\pi/2$ between voltage and driving-field signals) is the fingerprint of a hysteretic tracer material. In this case, image

reconstruction using a purely real SF, such as the one associated to Langevin particles, leads to unsatisfactory results.

In single-core magnetic tracers displaying frequency-sustained hysteresis the SF has been shown to remarkably depend on nanoparticle diameter because both shape and width of the hysteresis loop of a magnetic nanoparticle are strongly influenced by its size. Properly taking into account the complex effects of size on the third harmonic of the induced voltage is the key to explain why the efficiency and the spatial resolution of MPI do not increase monotonically with increasing nanoparticle diameter, as expected in the case of Langevin particles.

Tracer materials typically contain magnetic particles widely distributed in size, so that the target tissue can be populated by superparamagnetic tracers as well as by tracers, which display hysteresis at the operating frequency of MPI. Not taking into account the effect of the frequency-sustained hysteretic magnetization of the largest particles in the distribution leads to an inaccurate image reconstruction.

Often the nanoparticles used in diagnostic tools, such as MPI are considered to be noninteracting because of their low concentration in the tissue. However, dipole-dipole interaction is no longer negligible for larger nanoparticle concentrations, required, for instance, by specific therapeutic applications or occurring when tracers are accumulated in a small region of tissue. Dipole-dipole interaction is an intrinsic source of magnetic hysteresis whose effects combine with those of frequency. A glimpse of its impact on image reconstruction has been given using a simple model: as a first approximation, the SF of weakly interacting particles is shown to behave as the one of noninteracting particles of larger size. In the presence of a nonuniform spatial distribution of tracers, dipolar interaction (which depends on the local volume/surface fraction of particles) significantly affects image reconstruction. In the presence of a non-negligible dipolar interaction, considering the nanoparticles as entirely noninteracting definitely worsens the reconstructed image.

Finally, it should be mentioned that some available tracer materials are made of *multicore* particles, each individual magnetic unit being an aggregate of smaller nanoparticles (having typical diameters in the 5–7 nm range) with randomly distributed easy axes. In this way, the effective magnetic anisotropy of a multicore aggregate is substantially reduced by an averaging effect, so that the energy barrier between minima of the DWS is lower in a multicore aggregate than in a single-core particle of the same size; in a similar way, the critical radius for the onset of superparamagnetism in quasistatic conditions is displaced towards larger sizes. A comparison of the SF of 15-nm multicore particles resulting from random aggregation of smaller (5-nm) nanoparticles with the ones of single-core particles of the same size as well as

of 5-nm nanoparticles, showing the beneficial effect of clustering, can be found in Sec. S8 of the Supplemental Material [68]. Multicore particles owe their popularity as tracers for MPI to the fact that they combine a low effective anisotropy, a high saturation magnetization, and a $M(H)$ curve steeper than the one of the smaller component particles, which makes them quite responsive to the driving field. However, also multicore particles are affected by frequency-sustained hysteresis even if they are superparamagnetic in dc measurements.

Therefore, in these aggregates all the effects discussed in the present work—basically deriving from the loss of the superparamagnetic features at high frequency—are still present, so that our conclusions maintain their validity, with an obvious shift of all numerical results towards larger diameters.

APPENDIX

The surface fraction f_s of nanoparticles can be defined in two equivalent ways. By definition, $f_s = S_{\text{tot}}/L^2$, where S_{tot} is the total area resulting from the sum of all circular areas projected by the magnetite particles on the scanned plane. It is easy to prove that the surface fraction can also be written as $f_s = S/d^2$ where $S = (\pi/4)D^2$ is the area projected on the scanned plane by a single nanoparticle of diameter D and d is the average interparticle distance on the same plane. The quantity f_s takes values between 0 and $\pi/4 \simeq 0.785$, the upper limit corresponding to touching nanoparticles ($d = D$). Therefore, the ratio (d/D) is expressed as $(d/D) = \pi^{1/2}/(2f_s^{1/2})$. For a uniform distribution of particles with $f_s = 1 \times 10^{-4}$ one gets $(d/D) = 88.6$. For the Gaussian distribution of particles used in Sec. III, the surface fraction takes the value $f_s = 7 \times 10^{-4}$ inside the minor square region around the center, so that $(d/D) = 10.6$ there.

The parameters α_2, α appearing in Eqs. (2) and (3) contain the square root $A_6^{1/2}$ of the dimensionless sum $A_6 = \sum_n (1/a_{mn})^6$ extending over all neighbors of the mth particle, where $a_{mn} = (d_{mn}/d)$, d_{mn} being the distance of any particle n from the reference particle m ($n \neq m$) and d the average nearest-neighbor distance [82,84]. As an expedient approximation, the nanoparticles can be thought to be placed at the vertexes of a simple cubic lattice (in 3D) or a simple square lattice (in 2D). In this case A_6 takes the values 8.40 (3D) and 4.6 (2D), so that $\alpha_2/\alpha = (4.66/8.4)^{1/2} \simeq 0.745$.

[1] B. Gleich and J. Weizenecker, Tomographic imaging using the nonlinear response of magnetic particles, Nature **435**, 1214 (2005).

[2] K. Enpuku and T. Yoshida, *Bioimaging*, edited by S. Ueno (CRC Press, Boca Raton, 2020), Chap. 7, p. 155.

[3] S. Harvell-Smith, L. Tunga, and N. Thanh, Magnetic particle imaging: Tracer development and the biomedical applications of a radiationfree, sensitive, and quantitative imaging modality, Nanoscale **14,** 3658 (2021).

[4] S. J. Park, S. R. Han, Y. H. Kang, E. J. Lee, E. G. Kim, H. Hong, J. C. Jeong, M. S. Lee, S. H. Lee, and D. Y. Song, In vivo preclinical tumor-specific imaging of superparamagnetic iron oxide nanoparticles using magnetic particle imaging for cancer diagnosis, Int. J. Nanomedicine **17,** 3711 (2022).

[5] A. P. Khandhar, P. Keselman, S. J. Kemp, R. M. Ferguson, P. W. Goodwill, S. M. Conolly, and K. M. Krishnan, Evaluation of PEG-coated iron oxide nanoparticles as blood pool tracers for preclinical magnetic particle imaging, Nanoscale **9,** 1299 (2017).

[6] T. Knopp, N. Gdaniec, and M. Möddel, Magnetic particle imaging: From proof of principle to preclinical applications, Phys. Med. Biol. **62,** R124 (2017).

[7] X. Yang, G. Shao, Y. Zhang, W. Wang, Y. Qi, S. Han, and H. Li, Applications of magnetic particle imaging in biomedicine: Advancements and prospects, Front. Physiol. **13,** 898426 (2022).

[8] C. Billings, M. Langley, G. Warrington, F. Mashali, and J. A. Johnson, Magnetic particle imaging: Current and future applications, magnetic nanoparticle synthesis methods and safety measures, Int. J. Mol. Sci. **22,** 7651 (2021).

[9] N. Talebloo, M. Gudi, N. Robertson, and P. Wang, Magnetic particle imaging: Current applications in biomedical research, J. Magn. Reson. Imaging **51,** 1659 (2020).

[10] A. V. Makela, M. A. Schott, O. C. Sehl, J. J. Gevaert, P. J. Foster, and C. H. Contag, Tracking the fates of iron-labeled tumor cells in vivo using magnetic particle imaging, Nanoscale Adv. **4,** 3617 (2022).

[11] H. Arami, E. Teeman, A. Troksa, H. Bradshaw, K. Saatchi, A. Tomitaka, S. S. Gambhir, U. O. Häfeli, D. Liggitt, and K. M. Krishnan, Tomographic magnetic particle imaging of cancer targeted nanoparticles, Nanoscale **9,** 18723 (2017).

[12] P. Ludewig, M. Graeser, N. D. Forkert, F. Thieben, J. Rández-Garbayo, J. Rieckhoff, K. Lessmann, F. Förger, P. Szwargulski, T. Magnus, and T. Knopp, Magnetic particle imaging for assessment of cerebral perfusion and ischemia, Wiley Interdiscip. Rev.: Nanomed. Nanobiotechnol. **14,** e1757 (2022).

[13] A. C. Bakenecker, A. von Gladiss, H. Schwenke, A. Behrends, T. Friedrich, K. Lüdtke-Buzug, A. Neumann, J. Barkhausen, F. Wegner, and T. M. Buzug, Navigation of a magnetic micro-robot through a cerebral aneurysm phantom with magnetic particle imaging, Sci. Rep. **11,** 14082 (2021).

[14] A. Meola, J. Rao, N. Chaudhary, G. Song, X. Zheng, and S. D. Chang, Magnetic particle imaging in neurosurgery, World Neurosurg. **125,** 261 (2019).

[15] W. Tong, H. Hui, W. Shang, Y. Zhang, F. Tian, Q. Ma, X. Yang, J. Tian, and Y. Chen, Highly sensitive magnetic particle imaging of vulnerable atherosclerotic plaque with active myeloperoxidase-targeted nanoparticles, Theranostics **11,** 506 (2020).

[16] A. Mohtashamdolatshahi, H. Kratz, O. Kosch, R. Hauptmann, N. Stolzenburg, F. Wiekhorst, I. Sack, B. Hamm, M. Taupitz, and J. Schnorr, In vivo magnetic particle imaging: angiography of inferior vena cava and aorta in rats using newly developed multicore particles, Sci. Rep. **10,** 17247 (2020).

[17] H. Paysen, N. Loewa, A. Stach, J. Wells, O. Kosch, S. Twamley, M. R. Makowski, T. Schaeffter, A. Ludwig, and F. Wiekhorst, Cellular uptake of magnetic nanoparticles imaged and quantified by magnetic particle imaging, Sci. Rep. **10,** 1922 (2020).

[18] Z. W. Tay, P. Chandrasekharan, A. Chiu-Lam, D. W. Hensley, R. Dhavalikar, X. Y. Zhou, E. Y. Yu, P. W. Goodwill, B. Zheng, C. Rinaldi, and S. M. Conolly, Magnetic particle imaging-guided heating in vivo using gradient fields for arbitrary localization of magnetic hyperthermia therapy, ACS Nano **12,** 3699 (2018).

[19] P. Vogel, J. Markert, M. A. Rückert, S. Herz, B. Keßler, K. Dremel, D. Althoff, M. Weber, T. M. Buzug, T. A. Bley, W. H. Kullmann, R. Hanke, S. Zabler, and V. C. Behr, Magnetic particle imaging meets computed tomography: First simultaneous imaging, Sci. Rep. **9,** 12627 (2019).

[20] S. Healy, A. F. Bakuzis, P. W. Goodwill, A. Attaluri, J. W. Bulte, and R. Ivkov, Clinical magnetic hyperthermia requires integrated magnetic particle imaging, Wiley Interdiscip. Rev.: Nanomed. Nanobiotechnol. **14,** e1779 (2022).

[21] E. Y. Yu, M. Bishop, B. Zheng, R. M. Ferguson, A. P. Khandhar, S. J. Kemp, K. M. Krishnan, P. W. Goodwill, and S. M. Conolly, Magnetic particle imaging: A novel in vivo imaging platform for cancer detection, Nano Lett. **17,** 1648 (2017).

[22] A. Rivera-Rodriguez, L. B. Hoang-Minh, A. Chiu-Lam, N. Sarna, L. Marrero-Morales, D. A. Mitchell, and C. M. Rinaldi-Ramos, Tracking adoptive T cell immunotherapy using magnetic particle imaging, Nanotheranostics **5,** 431 (2021).

[23] E. Y. Yu, P. Chandrasekharan, R. Berzon, Z. W. Tay, X. Y. Zhou, A. P. Khandhar, R. M. Ferguson, S. J. Kemp, B. Zheng, P. W. Goodwill, M. F. Wendland, K. M. Krishnan, S. Behr, J. Carter, and S. M. Conolly, Magnetic particle imaging for highly sensitive, quantitative, and safe in vivo gut bleed detection in a murine model, ACS Nano **11,** 12067 (2017).

[24] P. Szwargulski, M. Wilmes, E. Javidi, F. Thieben, M. Graeser, M. Koch, C. Gruettner, G. Adam, C. Gerloff, T. Magnus, T. Knopp, and P. Ludewig, Monitoring intracranial cerebral hemorrhage using multicontrast real-time magnetic particle imaging, ACS Nano **14,** 13913 (2020).

[25] J. W. Bulte, Superparamagnetic iron oxides as MPI tracers: A primer and review of early applications, Adv. Drug. Deliv. Rev. **138,** 293 (2019).

[26] R. M. Ferguson, A. P. Khandhar, H. Arami, L. Hua, O. Hovorka, and K. M. Krishnan, Tailoring the magnetic and pharmacokinetic properties of iron oxide magnetic particle imaging tracers, Biomedizinische Technik **58,** 493 (2013).

[27] Z. W. Tay, S. Savliwala, D. W. Hensley, K. L. Fung, C. Colson, B. D. Fellows, X. Zhou, Q. Huynh, Y. Lu, B. Zheng, P. Chandrasekharan, S. M. Rivera-Jimenez, C. M. Rinaldi-Ramos, and S. M. Conolly, Superferromagnetic nanoparticles enable order-of-magnitude resolution & sensitivity gain in magnetic particle imaging, Small Methods **5,** 2100796 (2021).

[28] C. Saayujya, K. L. Fung, Q. Huynh, C. Colson, B. Fellows, P. Chandrasekharan, and S. M. Conolly, Computational modeling of superferromagnetism in finite-length chains of superparamagnetic iron oxide tracers for use in super-resolution magnetic particle imaging, Int. J. Magn. Part. Imaging **8,** 2203052 (2022).

[29] B. Zheng, M. P. Von See, E. Yu, B. Gunel, K. Lu, T. Vazin, D. V. Schaffer, P. W. Goodwill, and S. M. Conolly, Quantitative magnetic particle imaging monitors the transplantation, biodistribution, and clearance of stem cells in vivo, Theranostics **6,** 291 (2016).

[30] X. Zhu, J. Li, P. Peng, N. Hosseini Nassab, and B. R. Smith, Quantitative drug release monitoring in tumors of living subjects by magnetic particle imaging nanocomposite, Nano Lett. **19,** 6725 (2019).

[31] A. Bakenecker, M. Ahlborg, C. Debbeler, C. Kaethner, and K. Lüdtke-Buzug, *Precision Medicine: Tools and Quantitative Approaches*, edited by H.-P. Deigner and M. Kohl (Academic Press, Cambridge, Mass, 2018), Chap. 9, p. 183.

[32] K. Murase, Generation of system function maps in projection-based magnetic particle imaging using lock-in-amplifier model, arXiv:1901.04475 [physics.med-ph] , 1 (2019).

[33] J. Rahmer, J. Weizenecker, B. Gleich, and J. Borgert, Signal encoding in magnetic particle imaging: Properties of the system function, BMC Med. Imaging **9,** 4 (2009).

[34] J. Rahmer, J. Weizenecker, B. Gleich, and J. Borgert, Analysis of a 3-D system function measured for magnetic particle imaging, IEEE Trans. Med. Imaging **31,** 1289 (2012).

[35] O. Kosch, U. Heinen, L. Trahms, and F. Wiekhorst, Preparing system functions for quantitative MPI, Int. J. Magn. Part. Imaging **3,** 1706002 (2017).

[36] D. B. Mangarova, J. Brangsch, A. Mohtashamdolatshahi, O. Kosch, H. Paysen, F. Wiekhorst, R. Klopfleisch, R. Buchholz, U. Karst, M. Taupitz, J. Schnorr, B. Hamm, and M. R. Makowski, Ex vivo magnetic particle imaging of vascular inflammation in abdominal aortic aneurysm in a murine model, Sci. Rep. **10,** 12410 (2020).

[37] K. Murase and K. Shimada, Lock-in-amplifier model for analyzing the behavior of signal harmonics in magnetic particle imaging, Open J. Appl. Sci. **8,** 170 (2018).

[38] D. Pantke, N. Holle, A. Mogarkar, M. Straub, and V. Schulz, Multifrequency magnetic particle imaging enabled by a combined passive and active drive field feed-through compensation approach, Med. Phys. **46,** 4077 (2019).

[39] G. Barrera, P. Allia, and P. Tiberto, Magnetization Dynamics of Superparamagnetic Nanoparticles for Magnetic Particle Spectroscopy and Imaging, Phys. Rev. Appl. **18,** 024077 (2022).

[40] D. Henrard, Q. L. Vuong, S. Delangre, X. Valentini, D. Nonclercq, M. F. Gonon, and Y. Gossuin, Monitoring of superparamagnetic particle sizes in the Langevin law regime, J. Nanomater. **2019,** 6409210 (2019).

[41] M. Knobel, W. C. Nunes, L. M. Socolovsky, E. De Biasi, J. M. Vargas, and J. C. Denardin, Superparamagnetism and other magnetic features in granular materials: A review on ideal and real systems, J. Nanosci. Nanotechnol. **8,** 2836 (2008).

[42] S. Ziemian, N. Löwa, O. Kosch, D. Bajj, F. Wiekhorst, and G. Schütz, Optimization of iron oxide tracer synthesis for magnetic particle imaging, Nanomaterials **8,** 180 (2018).

[43] H. T. K. Duong, A. Abdibastami, L. Gloag, L. Barrera, J. J. Gooding, and R. D. Tilley, A guide to the design of magnetic particle imaging tracers for biomedical applications, Nanoscale **14,** 13890 (2022).

[44] C. Lu, L. Han, J. Wang, J. Wan, G. Song, and J. Rao, Engineering of magnetic nanoparticles as magnetic particle imaging tracers, Chem. Soc. Rev. **50,** 8102 (2021).

[45] P. Chandrasekharan, Z. W. Tay, D. Hensley, X. Y. Zhou, B. K. Fung, C. Colson, Y. Lu, B. D. Fellows, Q. Huynh, C. Saayujya, E. Yu, R. Orendorff, B. Zheng, P. Goodwill, C. Rinaldi, and S. Conolly, Using magnetic particle imaging systems to localize and guide magnetic hyperthermia treatment: Tracers, hardware, and future medical applications, Theranostics **10,** 2965 (2020).

[46] G. Barrera, P. Allia, and P. Tiberto, Magnetic nanoparticle imaging: Insight on the effects of magnetic interactions and hysteresis of tracers, ACS Appl. Nano Mater. **5,** 2699 (2022).

[47] G. Barrera, P. Allia, and P. Tiberto, Dipolar interactions among magnetite nanoparticles for magnetic hyperthermia: A rate-equation approach, Nanoscale **13,** 4103 (2021).

[48] A. S. Eggeman, S. A. Majetich, D. Farrell, and Q. A. Pankhurst, Size and concentration effects on high frequency hysteresis of iron oxide nanoparticles, IEEE Trans. Magn. **43,** 2451 (2007).

[49] C. Binns, *Nanomagnetism: Fundamentals and Applications*, edited by C. Binns (Elsevier, Oxford, 2014).

[50] E. Garaio, O. Sandre, J. M. Collantes, J. A. Garcia, S. Mornet, and F. Plazaola, Specific absorption rate dependence on temperature in magnetic field hyperthermia measured by dynamic hysteresis losses (ac magnetometry), Nanotechnology **26,** 015704 (2015).

[51] P. Allia, G. Barrera, and P. Tiberto, Nonharmonic Driving Fields for Enhancement of Nanoparticle Heating Efficiency in Magnetic Hyperthermia, Phys. Rev. Appl. **12,** 034041 (2019).

[52] J. Liu, B. Jang, D. Issadore, and A. Tsourkas, Use of magnetic fields and nanoparticles to trigger drug release and improve tumor targeting, Wiley Interdiscip. Rev.: Nanomed. Nanobiotechnol. **11,** e1571 (2019).

[53] M. Moros, J. Idiago-López, L. Asín, E. Moreno-Antolín, L. Beola, V. Grazú, R. M. Fratila, L. Gutiérrez, and J. M. de la Fuente, Triggering antitumoural drug release and gene expression by magnetic hyperthermia, Adv. Drug. Deliv. Rev. **138,** 326 (2019).

[54] I. Rodrigo, I. Castellanos-Rubio, E. Garaio, O. K. Arriortua, M. Insausti, I. Orue, J. Á. García, and F. Plazaola, Exploring the potential of the dynamic hysteresis loops via high field, high frequency and temperature adjustable AC magnetometer for magnetic hyperthermia characterization, Int. J. Hyperthermia **37,** 976 (2020).

[55] G. Barrera, P. Allia, and P. Tiberto, Temperature-dependent heating efficiency of magnetic nanoparticles for applications in precision nanomedicine, Nanoscale **12,** 6360 (2020).

[56] P. Goodwill and S. Conolly, The *x*-space formulation of the magnetic particle imaging process: 1-d signal, resolution, bandwidth, SNR, SAR, and magnetostimulation, IEEE Trans. Med. Imaging **29,** 1851 (2010).

[57] P. Allia, G. Barrera, and P. Tiberto, Linearized rate-equation approach for double-well systems: Cooling- and temperature-dependent low-field magnetization of magnetic nanoparticles, Phys. Rev. B **98,** 134423 (2018).

[58] X. Chen, Z. Jiang, X. Han, X. Wang, and X. Tang, The reconstruction of magnetic particle imaging: Current approaches based on the system matrix, Diagnositics **11,** 773 (2021).

[59] R. Di Corato, A. Espinosa, L. Lartigue, M. Tharaud, S. Chat, T. Pellegrino, C. Ménager, F. Gazeau, and C. Wilhelm, Magnetic hyperthermia efficiency in the cellular environment for different nanoparticle designs, Biomaterials **35,** 6400 (2014).

[60] D. Soukup, S. Moise, E. Céspedes, J. Dobson, and N. D. Telling, *In situ* measurement of magnetization relaxation of internalized nanoparticles in live cells, ACS Nano **9,** 231 (2015).

[61] S. Dutz and R. Hergt, Magnetic particle hyperthermia - A promising tumour therapy?, Nanotechnology **25,** 452001 (2014).

[62] M. Shliomis, Magnetic fluids, Sov. Phys. - Uspekhi **17,** 153 (1974).

[63] N. A. Usov, Numerical simulation of field-cooled and zero field-cooled processes for assembly of superparamagnetic nanoparticles with uniaxial anisotropy, J. Appl. Phys. **109,** 023913 (2011).

[64] C. Shasha, E. Teeman, and K. M. Krishnan, Nanoparticle core size optimization for magnetic particle imaging, Biomed. Phys. Eng. Express **5,** 055010 (2019).

[65] P. Allia, G. Barrera, and P. Tiberto, Hysteresis effects in magnetic nanoparticles: A simplified rate-equation approach, J. Magn. Magn. Mater. **496,** 165927 (2020).

[66] N. A. Usov, E. M. Gubanova, and Z. H. Wei, Specific absorption rate of assembly of magnetic nanoparticles with uniaxial anisotropy, J. Phys.: Conf. Ser. **1439,** 012044 (2020).

[67] G. Barrera, P. Allia, and P. Tiberto, Fine tuning and optimization of magnetic hyperthermia treatments using versatile trapezoidal driving-field waveforms, Nanoscale Adv. **2,** 4652 (2020).

[68] See Supplemental Material at http://link.aps.org/supplemental/10.1103/PhysRevApplied.19.034029 for a summary of the rate-equation framework; time behavior of magnetization; minor hysteresis loops; system function for different nanoparticle diameters; effect of dipolar interaction; image reconstruction under a 6 T/m magnetic field gradient; phantom particles; multicore versus single-core particles.

[69] Z. W. Tay, D. W. Hensley, E. C. Vreeland, B. Zheng, and S. M. Conolly, The relaxation wall: experimental limits to improving MPI spatial resolution by increasing nanoparticle core size, Biomed. Phys. Eng. Express **3,** 035003 (2017).

[70] G. Barrera, P. Allia, and P. Tiberto, Heating ability modulation by clustering of magnetic particles for precision therapy and diagnosis, J. Phys. D: Appl. Phys. **54,** 315003 (2021).

[71] R. Ferguson, K. Minard, and K. Krishnan, Optimization of nanoparticle core size for magnetic particle imaging, J. Magn. Magn. Mater. **321,** 1548 (2009).

[72] A. P. Ferguson, R. M. Khandhar, K. R. Minard, and K. Krishnan, *Magnetic nanoparticles*, edited by T. M. Buzug, J. Borgert, T. Knopp, S. Biederer, T. F. Sattel, M. Erbe, and K. Lüdtke-Buzug (World Scientific Publishing Co. Pte. Ltd., Singapore, 2010), p. 53.

[73] S. Ota, R. Takeda, I. Kato, S. Nohara, and Y. Takemura, Effect of particle size and structure on harmonic intensity of blood-pooling multi-core magnetic nanoparticles for magnetic particle imaging, Int. J. Magn. Part. Imaging **3,** 1703003 (2017).

[74] T. Jiang, W. Yi, Z. Du, and W. Liu, An improved point spread function for complex susceptibility-based magnetic particle imaging, Meas. Sci. Technol. **33,** 095402 (2022).

[75] Z. W. Tay, D. W. Hensley, P. Chandrasekharan, B. Zheng, and S. M. Conolly, Optimization of drive parameters for resolution, sensitivity and safety in magnetic particle imaging, IEEE Trans. Med. Imaging **39,** 1724 (2020).

[76] O. C. Sehl, J. J. Gevaert, K. P. Melo, N. N. Knier, and P. J. Foster, A perspective on cell tracking with magnetic particle imaging, Tomography **6,** 315 (2020).

[77] K.-J. Janssen, M. Schilling, F. Ludwig, and J. Zhong, Single harmonic-based narrowband magnetic particle imaging, Meas. Sci. Technol. **33,** 095405 (2022).

[78] P. Szwargulski, M. Moddel, N. Gdaniec, and T. Knopp, Efficient joint image reconstruction of multi-patch data reusing a single system matrix in magnetic particle imaging, IEEE Trans. Med. Imaging **38,** 932 (2019).

[79] F. Mohn, T. Knopp, M. Boberg, F. Thieben, P. Szwargulski, and M. Graeser, System matrix based reconstruction for pulsed sequences in magnetic particle imaging, IEEE Trans. Med. Imaging **41,** 1862 (2022).

[80] K. Gräfe, A. Von Gladiss, G. Bringout, M. Ahlborg, and T. M. Buzug, 2D images recorded with a single-sided magnetic particle imaging scanner, IEEE Trans. Med. Imaging **35,** 1056 (2016).

[81] It should be recalled that in the examined cases the reconstructed $c^*(r_i)$ distribution is a complex function of space.

[82] S. Morup, Superparamagnetism and spin glass ordering in magnetic nanocomposites, Europhys. Lett. **28,** 671 (1994).

[83] B. D. Cullity and C. D. Graham, *Introduction to Magnetic Materials* (Wiley, Hoboken, N.J., 2009).

[84] S. Mørup and E. Tronc, Superparamagnetic Relaxation of Weakly Interacting Particles, Phys. Rev. Lett. **72,** 3278 (1994).